nature catalysis

Article

https://doi.org/10.1038/s41929-022-00844-w

Exploration of the bio-analogous asymmetric C–C coupling mechanism in tandem CO_2 electroreduction

Received: 5 April 2022

Accepted: 18 August 2022

Published online: 29 September 2022

Check for updates

Chubai Chen[1,2,6], Sunmoon Yu[2,3,6], Yao Yang[1,4], Sheena Louisia[1,2], Inwhan Roh[1], Jianbo Jin[1], Shouping Chen[2,3], Peng-Cheng Chen[1,5], Yu Shan[2,3] and Peidong Yang[1,2,3,5]

C–C coupling is a critical step of CO_2 fixation in constructing the carbon skeleton of value-added multicarbon products. The Wood–Ljungdahl pathway is an efficient natural process through which microbes transform CO_2 into methyl and carbonyl groups and subsequently couple them together. This asymmetric coupling mechanism remains largely unexplored in inorganic CO_2 electroreduction. Here we experimentally validate the asymmetric coupling pathway through isotope-labelled co-reduction experiments on a Cu surface where $^{13}CH_3I$ and ^{12}CO are co-fed externally as the methyl and the carbonyl source, respectively. Isotope-labelled multicarbon oxygenates were detected, which confirms an electrocatalytic asymmetric coupling on the Cu surface. We further employed tandem Cu–Ag nanoparticle systems in which $*CH_x$ and *CO intermediates can be generated to achieve asymmetric C–C coupling for a practical CO_2 electroreduction. We found that the production of multicarbon oxygenates is correlated with the generation rate of two intermediate indicators, CH_4 and CO. By aligning their rates, the oxygenates generation rate can be maximized.

The electrochemical carbon dioxide reduction reaction (CO_2RR) was regarded as a promising technology to help achieve carbon neutrality before 2070[1]. Therefore, a wide range of research was stimulated with the aim to convert CO_2 into value-added multicarbon chemicals with more control over the catalytic selectivity[2–5]. However, as a principal step in constructing carbon skeletons, the C–C coupling mechanism in CO_2 fixation chemistry still needs further investigation as it is not yet well understood.

Interestingly, some bacteria in nature can digest CO_2 through the Wood–Ljungdahl (WL) metabolic pathway and efficiently transform it into acetate with complete selectivity. In the past decades, extensive research efforts were undertaken to reveal the underlying mechanisms of CO_2 transformation and C–C coupling in the WL pathway, and a molecular-level understanding was established[6,7]. CO_2 molecules are first converted into methyl groups and carbonyl groups in the western and eastern branches of this pathway, respectively. These two groups then go through asymmetric C–C coupling with the assistance of acetyl-coenzyme-A (acetyl-CoA) synthase, which results in acetate production (Fig. 1a).

For direct CO_2 electroreduction, Cu has attracted substantial attention as a catalyst among the many other inorganic materials as it is the only metal that can activate C–C coupling and therefore generate products beyond C_1 chemistry (C_2H_4, C_2H_5OH, CH_3COOH, n-C_3H_7OH and so on). However, owing to the complexity of CO_2 reduction on the Cu surface, understanding the coupling process on the Cu surface is still regarded as one of the central challenges in CO_2RR after decades

[1]Department of Chemistry, University of California, Berkeley, CA, USA. [2]Chemical Sciences Division, Lawrence Berkeley National Laboratory, Berkeley, CA, USA. [3]Department of Materials Science and Engineering, University of California, Berkeley, CA, USA. [4]Miller Institute for Basic Research in Science, University of California, Berkeley, CA, USA. [5]Kavli Energy NanoScience Institute, Berkeley, CA, USA. [6]These authors contributed equally: Chubai Chen, Sunmoon Yu. e-mail: p_yang@berkeley.edu

https://doi.org/10.1038/s41929-022-00844-w

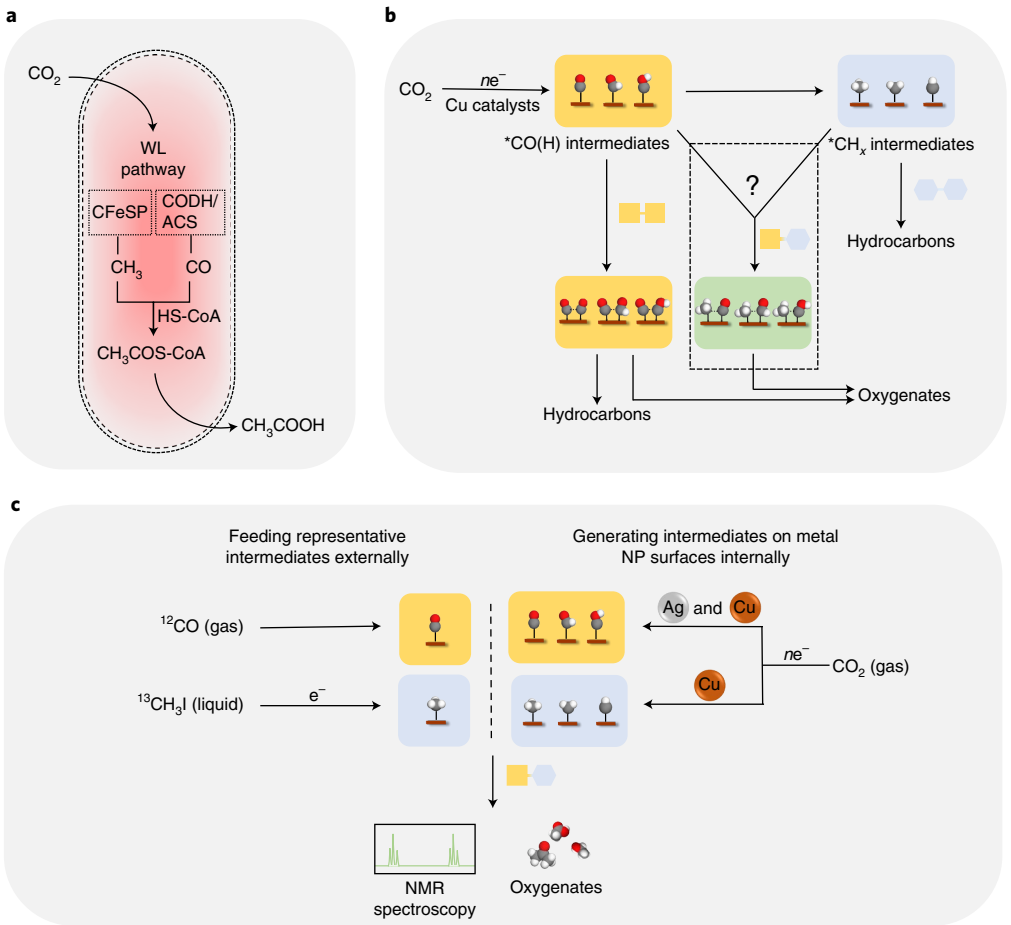

Fig. 1 | Asymmetric C–C coupling pathways in biological carbon fixation and inorganic CO_2 electroreduction. a, Schematic illustration of $*CH_3$–*CO asymmetric coupling in the WL pathway as a natural CO_2 biofixation process. In the WL pathway, corrinoid iron–sulfur protein (CFeSP) delivers a methyl group derived from CO_2 to carbon monoxide dehydrogenase (CODH)/acetyl-CoA synthase (ACS) whereby CO_2 is converted into *CO and further combined with $*CH_3$ and coenzyme-A (CoA), which leads to the synthesis of acetyl-CoA (CH_3COS-CoA) and finally the generation of acetic acid. **b**, Schematic illustration of symmetric and underexplored asymmetric coupling process in inorganic CO_2 electroreduction. **c**, In this study, isotope-labelled intermediates were externally fed to verify the existence of the asymmetric coupling process on a Cu surface. Afterward, a Cu–Ag nanoparticle (NP) assembly was used to generate asymmetric coupling intermediates internally in the CO_2 electroreduction, which demonstrated the feasibility of the asymmetric C–C coupling mechanism in CO_2 reduction with inorganic catalysts.

of research[2,8]. Currently, it is widely accepted that carbon monoxide (CO) generated from CO_2RR is the key intermediate for symmetric C–C coupling[9,10]. One compelling experimental evidence is that the potential window and product spectrum of both CO reduction and CO_2 reduction show a high degree of consistency[11]. Nevertheless, there is still a lack of a comprehensive and convincing molecular picture of such a C–C coupling. Although some density functional theory calculations and in situ spectroscopic evidence support the direct CO–CO dimerization on the Cu surface (*CO–*CO)[12–14], some other reports indicate that the protonation of *CO towards either hydroxymethylidyne (*COH) or formyl (*CHO) prior to C–C coupling is more thermodynamically favoured under an acidic to neutral pH[15–17]. Accordingly, *COH or *CHO could participate in the downstream C–C coupling. However, the exact role of these two intermediates is also debatable[16,18–20]. The lack of consensus can be attributed to several factors: a substantial dependence of density functional theory results on modelling and algorithms, and the non-negligible impact of experimental conditions associated with the catalytic sensitivity, which include but are not limited to applied potentials, surface pH, Cu active sites, electrolyte species and surface modifiers within the double layer[21–25].

Although the asymmetric coupling between *CO and *CHO (*COH) was explored for CO_2RR, very few of the efforts go further to discuss the possibility of the WL-pathway-like $*CH_3$ and *CO coupling in inorganic aqueous CO_2 electrolysis. One important reason why the study of asymmetric coupling is hampered is the challenge in correlating the experimentally detected $*CH_x$ ($x = 1$–3) signals in the operando spectrum to any particular intermediate or process[26,27]. Recently, some studies proposed that the $*CH_x$–*CO asymmetric coupling may happen under a CO-concentrated environment (either generated by the tandem catalyst architectures[28,29] or the high-pressure CORR[30]) and contribute to the final product selectivity. The feasibility of asymmetric $*CH_x$–*CO coupling was theoretically studied and found to be energetically and kinetically possible on some specific Cu sites[28,29]. Nevertheless, without firm experimental evidence, it is still uncertain whether Cu has the ability to achieve asymmetric coupling on its surface during aqueous CO_2 electrolysis. The product spectrum of asymmetric coupling and the corresponding conversion mechanism is also unclear at this point.

Here we designed co-reduction experiments to verify the catalytic capability of Cu surfaces for asymmetric $*CH_3$–*CO coupling by using an electropolished Cu foil. To circumvent the dilemma that it is difficult to specify intermediates from the spectrum, we assured the existence of the intermediates by externally feeding CO and CH_3I as the two distinct intermediate sources. *CO comes from the adsorption of CO gas, while $*CH_3$ is electrochemically generated from CH_3I. By further

https://doi.org/10.1038/s41929-022-00844-w

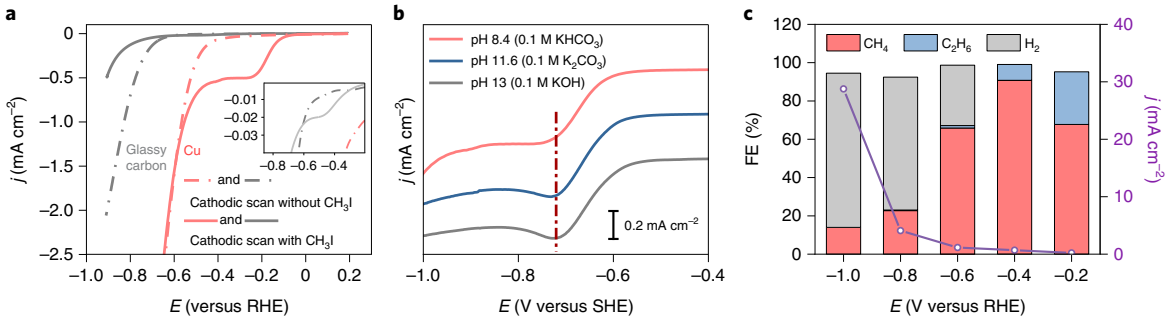

Fig. 2 | Electrocatalytic dehalogenation of CH_3I under negative biases. a, The polarization response curve on the EC-Cu and glassy carbon electrodes with and without CH_3I in 0.1 M $KHCO_3$. **b**, The pH independence of the characteristic CH_3I reduction peak position on EC-Cu against the SHE scale. **c**, Potential-dependent FE of different CH_3IRR products and their corresponding current densities during CH_3I electroreduction on EC-Cu.

labelling CH_3I with the ^{13}C isotope, the verification of ^{13}C–^{12}C asymmetric coupling became technically feasible via NMR spectroscopy. During the electrolysis of CH_3I, we found that a portion of the generated methyl group can be stabilized on the Cu surface even in a highly polar aqueous electrolyte. These methyl groups can then participate in the C–C coupling reaction and be coupled with another $*CH_3$ or *CO to generate several multicarbon products (C_2H_6, CH_3CHO, C_2H_5OH, CH_3COOH and $(CH_3)_2CO$) on the Cu surface. After the asymmetric coupling ability of Cu was confirmed, we moved to a more practical CO_2 reduction electrocatalysis with a tandem Cu–Ag nanoparticle (NP) assembly. Analogous to the WL pathway, Cu is responsible for the $*CH_x$ intermediate generation and Ag is for most of the *CO in this tandem system. As it is a major challenge to quantify directly the concentration of the intermediates on the Cu surface under dynamic electrochemical conditions[31], we utilized the production rates of CH_4 and CO as a proxy for the availability of the $*CH_x$ and *CO intermediates in the catalytic microenvironment. The rate of CH_4 and CO production can be tuned by changing the Cu–Ag ratio and the applied potential. The maximum multicarbon oxygenate generation rate was achieved when the CH_4 and CO production rates were aligned.

Results

Dehalogenation of CH_3I on an electrified Cu surface

To investigate asymmetric $*CH_3$–*CO coupling on the Cu surface (Fig. 1b,c), electrochemically polished Cu foil (EC-Cu) was chosen as a model Cu catalyst for the co-reduction experiments. The representative surface morphology of the Cu foil before and after the electrochemical polish (Supplementary Fig. 1a,b) was characterized by scanning electron microscopy (SEM). It was found that most of the rough features on the pristine Cu foil disappeared after the polish, which gave a smoother surface. Meanwhile, double-layer capacitance measurements showed that the specific capacitance of EC-Cu decreased from 187.8 to 54.3 μF cm^{-2} (Supplementary Fig. 1c), which is a typical value for EC-Cu and is consistent with that of the previous reports[32]. Elemental information of EC-Cu was also collected through X-ray photoelectron spectroscopy (XPS) to track the potential contamination after electrolysis (Supplementary Fig. 2). The only increased signals can be attributed to the surface-absorbed iodine that stems from the electrolysis of CH_3I.

Alkyl halides are widely used as alkylating reagents in organic[33] and electroorganic[34] synthesis. Specifically, CH_3I was selected as the methyl-providing reagent in this study, given the solubility of CH_3I in aqueous electrolyte, the convenience of reaction product analysis and the fact that the electrochemical dehalogenation process of CH_3I on metal foils was also preliminarily reported[35]. By monitoring the composition of the gas effluent, we confirmed that no gas-phase product was generated through thermochemical processes, such as radical reactions, when CH_3I and EC-Cu coexisted in an aqueous electrolyte under an open-circuit potential (Supplementary Fig. 3).

The polarization response curve of the CH_3I reduction reaction (CH_3IRR) on EC-Cu was first explored to examine the potential window of in situ methyl generation in our system (Fig. 2a). Unlike the background curve representative of the hydrogen evolution reaction (HER) under an Ar atmosphere, the addition of CH_3I generated a distinctively strong electroreduction peak. The onset potential was around −0.1 V versus the reversible hydrogen electrode (RHE). It is worth noting that Cu does not behave as an inert electrode, but exhibits its catalytic behaviour towards CH_3IRR. The onset potential of the same reaction on a glassy carbon electrode is more than 200 mV negative along with a much smaller cathodic peak relative to that on Cu. The higher dissociation kinetics of CH_3I on the Cu surface may be attributed to the affinity between Cu and I (ref. [36]).

To further explore the influence of electrolysis-induced surface pH variation, a pH-dependent CH_3IRR was also conducted (Fig. 2b). No noticeable peak shift was observed against the scale of a standard hydrogen electrode (SHE) when the electrolyte was changed from 0.1 M $KHCO_3$ to 0.1 M K_2CO_3 and 0.1 M KOH, which indicates that any proton concentration effect on CH_3I dissociation, if existent, is negligible. Chronoamperometry experiments were then used to further study the potential dependency of CH_3IRR. The reduction products were collected and identified by gas chromatography (GC) and NMR spectroscopy. We found that CH_4 and C_2H_6 were the only two products generated from CH_3IRR (Fig. 2c), whereas H_2 and CH_3OH were by-products derived from the HER and CH_3I hydrolysis, respectively. It was also found that the production ratio between C_2H_6 and CH_4 was potential dependent. At −0.2 V versus RHE, a 67.7% Faraday efficiency (FE) towards CH_4 and a 27.5% FE towards C_2H_6 were achieved. The C_2H_6 FE decreased down to 0% when −1.0 V versus RHE was applied and HER became a dominant reaction. This observation suggests that the methyl generation and C–C coupling were likely to be mediated by the Cu surface—although the C–C coupling step may be a non-electrochemical process—while competing with the H_2 evolution. It is worth noting that CH_3I is not the only reagent that can be electrochemically reduced to a methyl group on a Cu surface. Generally, we believe that $*CH_x$ can be generated by electrochemical dehalogenation reactions of various halomethanes and polyhalomethanes under similar conditions[37].

Asymmetric coupling in $^{13}CH_3I$ and ^{12}CO co-reduction

CO was then introduced into the electrolysis system as another important building block in C–C asymmetric coupling on a Cu surface. As a reference, the CO self-coupling ability on EC-Cu within the potential window from −0.2 to −1.0 V versus RHE is also shown in Fig. 3a. Owing to the low solubility and inert property of CO in a 0.1 M $KHCO_3$ electrolyte[11], multicarbons generated from the CO reduction reaction (CORR) can only be detected under potentials more negative than −0.8 V versus RHE and the total FE towards CORR is less than 10%. Despite being minor products, the liquid product signals from CO self-coupling (Fig. 3b)

can still introduce uncertainty if they are not appropriately differentiated from the signals of the CH_3–CO asymmetric coupling products.

The introduction of a reactant labelled with the ^{13}C isotope into the experiment is an effective method to remove this uncertainty. Specifically, the presence of a ^{13}C atom induces the characteristic coupling to the surrounding protons and makes them distinguishable in the ^1H NMR spectrum. The co-reduction experiments were executed with ^{12}CO gas and liquid-phase $^{13}CH_3I$ as the starting chemicals. No new gas product was observed with GC. With similar product species and potential dependency, the gas product spectrum appears to result from the combination of $^{13}CH_3IRR$ and $^{12}CORR$ (Fig. 3c). Nevertheless, several sets of the new proton peaks previously absent in the CORR-only spectrum were identified in the NMR spectrum, which were rigorously assigned to the four multicarbon oxygenates generated through $^{13}CH_3$–^{12}CO asymmetric coupling (Fig. 3e). Importantly, these asymmetric coupling products do not show up under the open circuit potential with all other conditions kept the same. These results indicate that this co-reduction reaction is an electrocatalytic process and the corresponding equations are proposed in equations (1)–(4):

$$^*CH_3 + {}^*CO + H_2O + e^- \xrightarrow{\text{electrolysis on Cu}} CH_3CHO + OH^- \quad (1)$$

$$^*CH_3 + {}^*CO + 3H_2O + 3e^- \xrightarrow{\text{electrolysis on Cu}} CH_3CH_2OH + 3OH^- \quad (2)$$

$$2{}^*CH_3 + {}^*CO \xrightarrow{\text{electrolysis on Cu}} (CH_3)_2CO$$

or (3)

$$^*CH_3 + {}^*CO + CH_3I + e^- \xrightarrow{\text{electrolysis on Cu}} (CH_3)_2CO + I^-$$

$$^*CH_3 + {}^*CO + H_2O \xrightarrow{\text{electrolysis on Cu}} CH_3COOH + {}^*H \quad (4)$$

The potential-dependent generation amounts of isotope-labelled multicarbon oxygenates were also quantified to further understand the asymmetric coupling process (Fig. 3d). We found that the multicarbon oxygenate production amounts that resulted from asymmetric coupling after 6 hours of electrolysis first increase from 310 to 1,972 nmol cm^{-2} Cu when the applied potential was switched from −0.2 to −0.8 V versus RHE, as the CH_3IRR partial current density increases and the absorption of CO on Cu also becomes stronger[38,39]. A further increase in the applied potential to −1.0 V versus RHE inhibited the asymmetric coupling. This can be attributed to the overwhelming HER and competitive CORR pathways. Acetaldehyde (CH_3CHO) was a major product in the co-reduction experiments under the wide potential range, generated by either the hydrogenation of $^*CH_3$–$^*CO$ asymmetric coupling intermediate or the coupling between $^*CH_3$ and $^*CHO$. Based on the observations from CH_3IRR and CORR (Figs. 2c and 3a) and the spectroscopical evidence in the literature[14,18], the hydrogenation of CO requires a large overpotential. Therefore, the coupling between $^*CH_3$ and $^*CO$ is more likely to be the first step. Ethanol (CH_3CH_2OH) was found to be another asymmetric coupling product that existed from −0.6 to −1.0 V versus RHE, which can come from the further electroreduction of CH_3CHO (ref[40]). It is worth noting that although H_2O is illustrated as one of the proton sources in equations (1) and (2), the proton can be actually more broadly derived from bicarbonate and $^*H$ in HER.

Acetic acid (CH_3COOH) and acetone ($(CH_3)_2CO$) were also found as two minor products from the isotope-labelled co-reduction experiments. Instead of being hydrogenated, acetic acid and acetone were produced through further coupling processes between the $^*CH_3$–$^*CO$ intermediate with H_2O or $^*CH_3$ and/or CH_3I. Although the generation amounts of CH_3COOH and $(CH_3)_2CO$ were influenced by the applied potential, they were not as potential sensitive as CH_3CHO and CH_3CH_2OH. Nevertheless, it is worth noting that the CO (or CO_2) insertion-type reaction mechanism with $^*CH_x$ was previously proposed for acetic acid and acetone formation in thermal catalysis[41–43]. To verify whether CO_2 can also directly participate in the asymmetric coupling process with $^*CH_3$ as an alternative pathway to generate acetate, potential-dependent $^{12}CO_2$ and $^{13}CH_3I$ co-reduction experiments were also conducted (Supplementary Fig. 4). Interestingly, no ^{13}C-labelled acetate can be observed in these experiments, which indicates the coupling between $^*CH_3$ and CO_2 or $^*CO_2^{\cdot-}$ was prohibited. We propose that free CO_2 molecules have a linear configuration, which has a large steric hindrance, and so need to go through an Eley–Rideal insertion mechanism, which still requires a large activation energy. Meanwhile, the activated $^*CO_2^{\cdot-}$ on the electrified catalyst surface can be transformed into downstream intermediates quickly[44]. More mechanistic work is desired in the future to solidify these reaction mechanisms.

Meanwhile, free I^- was generated during the CH_3I reduction process, which may interfere with the Cu surface property and play a role in the co-reduction reaction[18]. To verify the potential influence of I^- in the system, a control CORR experiment was conducted in which KI was added to the electrolyte (0.1 M $KHCO_3$) to match up the theoretical I^- concentration with that in co-reduction reactions. As exhibited in Supplementary Fig. 5, no notable improvement in the multicarbon generation amount was found in this KI-added CORR experiment. Although the current result cannot completely preclude all the possible positive effects of the trace amount of surface-adsorbed iodine, it confirmed that this trace amount of the I^- in the system does not influence the isotope-labelled co-reduction experiment results.

Optimizing tandem CO_2 electrolysis via asymmetric coupling

The co-reduction experiments using two individual intermediates sources combined with isotope labelling provided us with strong evidence on the $^*CH_3$–$^*CO$ asymmetric coupling in a model EC-Cu system. We then further extended the research objectives from the exploration of a model-system-based mechanism to practical CO_2 electrolysis with nanocatalysts to advance our understanding of asymmetric coupling. To this end, a Cu–Ag bimetallic NP assembly was employed as the catalytic platform to explore the asymmetric coupling in CO_2RR. The colloidal synthesis of both 7 nm Cu and 7 nm Ag NPs followed our group's previously developed methods[44–46]. As an electrochemical tandem design principle, Ag can serve as a CO generator and Cu as a $^*CH_x$ generator[28,29] (equivalent to carbonyl and methyl branches, respectively, in the WL pathway) for such asymmetric coupling. According to previous research, the Cu NPs on glassy carbon exhibit a high selectivity towards methane[47], whereas Ag NPs were found to be a good CO-producing catalyst with nearly unity FE[44]. Although it is hard to directly probe the intermediates on the Cu during electrolysis, CO- and CH_4-generation rates can be easily measured and serve as an alternative way to indirectly monitor the corresponding surface chemistry. Therefore, we chose a potential range over which Ag NPs selectively produced CO and Cu NP-generated CH_4 as the main product.

The prepared monodisperse 7 nm Cu NPs (Fig. 4a) and Ag NPs (Fig. 4b) were spin coated onto a glassy carbon electrode to form a dense monolayer, which was then used for CO_2RR (Fig. 4c). Post-electrolysis characterization of the Cu–Ag NPs was also conducted to explore any other possible factors besides the tandem effect that may influence the catalytic performance. SEM imaging, scanning transmission electron microscopy (STEM) imaging, together with energy dispersive and electron energy loss spectroscopy (EDX and EELS) elemental mapping, showed that Cu NPs migrated and agglomerated to form a network during the CO_2 electrolysis due to the dynamic nature of Cu NPs (Supplementary Figs. 6 and 7). Ag particles were found to grow larger but remain isolated on the Cu–Ag network. The nanodomains and the interfaces between Ag and Cu were further characterized by high-resolution transmission electron microscopy (Supplementary Fig. 8). These results suggested that the Cu and Ag domains were in

https://doi.org/10.1038/s41929-022-00844-w

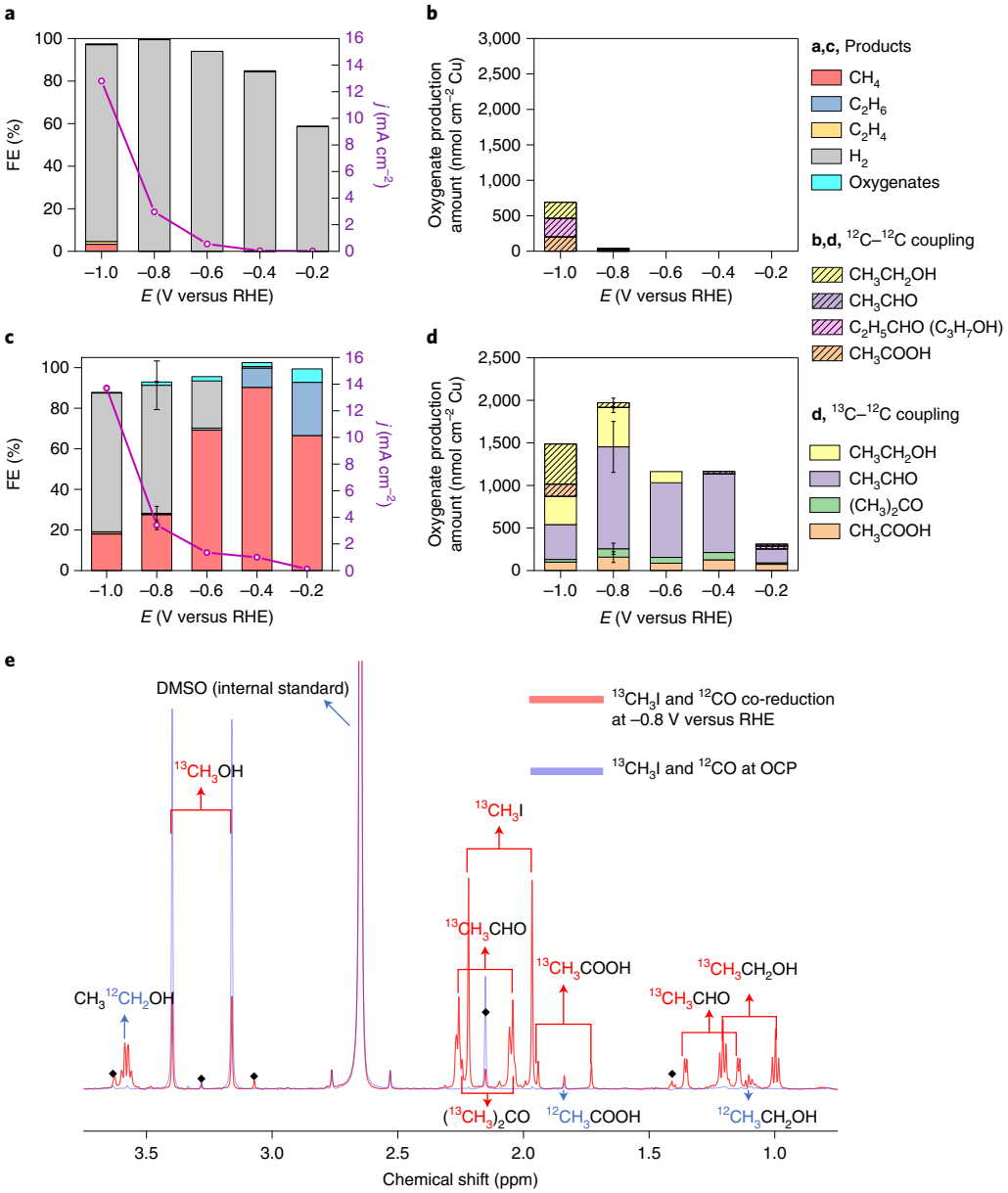

Fig. 3 | Potential dependent CO reduction experiments and $^{13}CH_3I$ and ^{12}CO co-reduction experiments on EC-Cu. a,**b**, Potential-dependent product FEs and corresponding current density (**a**) and multicarbon oxygenate production amounts and distribution after 6 h of electrolysis (**b**) for CO electroreduction on EC-Cu. **c**,**d**, Potential-dependent product FEs and corresponding current density (**c**) and multicarbon oxygenate production amounts and distribution after 6 h of electrolysis (**d**) for ^{12}CO and $^{13}CH_3I$ co-reduction on EC-Cu. Asymmetric products are quantified by isotope experiments. Error bars represent standard deviations based on three separate experiments, with the centre being the mean. The loss of FE under −0.2 and −0.4 V versus RHE in the CORR is due to the low current densities on EC-Cu. **e**, NMR spectra of the liquid products from $^{13}CH_3I$ and ^{12}CO co-reduction experiments. The identified peaks are labelled with the corresponding products. Blue highlights the products and/or protons that are related to ^{12}C and red those related to ^{13}C. The unidentified minor peaks are labelled with diamond marks, which may come from trace impurities in the CH_3I reagent and CH_3I-induced leaching of the rubber sealing components. It is clear that no coupling reaction happens at the open circuit potential, which shows a flat baseline. $^{13}CH_3OH$ mainly comes from the hydrolysis of $^{13}CH_3I$, which is not the target product in this study.

close contact with each other during CO_2RR rather than spatially separated on the as-prepared glassy carbon electrode. The XPS spectra of Cu and Ag indicated that no appreciable electronic interaction between Cu and Ag existed (Supplementary Fig. 9)[48].

Although $*CH_3$ generation in the co-reduction experiments can happen at potentials as positive as −0.1 V versus RHE due to external feeding of the CH_3I reagent, the hydrodeoxygenation of *CO intermediates to give $*CH_x$ intermediates on Cu during the CO_2RR usually happens under relatively negative potentials. The pure Cu NP assembly, which is denoted as Cu100, was found to produce a large amount of CH_4 within the potential window from −1.05 to −1.35 V versus RHE (Fig. 4d). A maximum CH_4 production rate of 4.66 nmol s^{-1} was achieved at −1.2 V versus RHE. When a more negative potential was applied, the overwhelming HER suppressed the CO_2 chemistry on Cu. Taking advantage of the tandem strategy, a certain fraction of the Cu NPs was replaced with Ag NPs to tune the catalytic CO_2 transformation rates towards both CO and CH_4. By increasing the Ag NP ratio from 0 to 50%, the CO generation rate at −1.2 V versus RHE was enhanced from 0.22 to 2.95 nmol s^{-1}. Meanwhile, as CO is a key intermediate in the production of CH_4 and functions as a competing adsorbate that suppresses HER,

https://doi.org/10.1038/s41929-022-00844-w

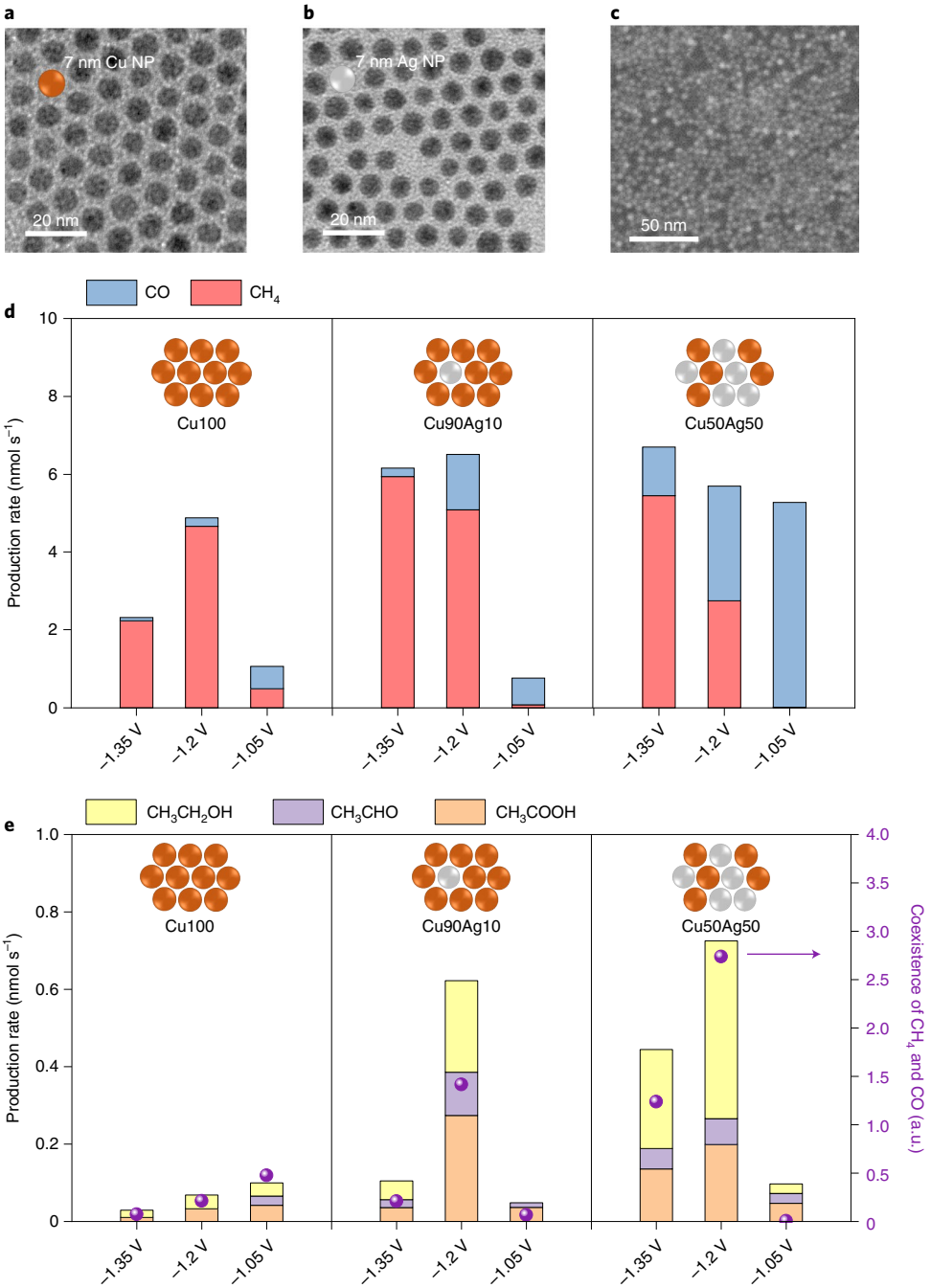

Fig. 4 | Cu–Ag tandem CO_2 electrolysis optimization via asymmetric coupling. a,**b**, TEM images of 7 nm Cu NPs (**a**) and 7 nm Ag NPs (**b**). **c**, SEM image of the as-prepared Cu–Ag NP assembly on glassy carbon as the working electrode. **d**, Potential-dependent production rates of CO and CH_4 as two intermediate indicators of CO_2 reduction on the Cu–Ag NP assembly electrodes with varied Cu–Ag ratios. **e**, Potential-dependent multicarbon oxygenate production rates in CO_2 reduction on Cu–Ag NP assembly electrodes with varied Cu–Ag ratios. The coexistence of CH_4 and CO is a dimensionless indicator defined as the minimum value between the CO and CH_4 production rates, which indicates the limiting factor for asymmetric coupling. All potentials here are described against the RHE scale. a.u., arbitrary units.

the generation of CH_4 on Cu sites may also benefit from the addition of Ag, especially under relatively negative potentials.

An aligned production rate of CO and CH_4 was achieved with Cu50Ag50 at −1.2 V versus RHE. Under such conditions, a 0.73 nmol s^{-1} production rate towards multicarbon oxygenates was observed on Cu50Ag50, 9.6 times higher than that on Cu100. To corroborate the early observation in the isotope co-reduction experiments, the correlation between multicarbon oxygenate production rates in tandem CO_2RR and the production rate of CO and CH_4 were also analysed (Fig. 4e). Considering the asymmetric coupling needs both *CO and *CH_x intermediates on the Cu surface, we defined the lower value between the CO and CH_4 production rates under a particular reaction condition as a rate-determining dimensionless indicator to describe the coexistence of CH_4 and CO. Taking CO_2RR on Cu50Ag50 as an example, the production rates of CO and CH_4 under −1.2 V versus RHE were 2.75 and 2.95 nmol s^{-1}, respectively. Therefore, the value that represents the coexistence of CH_4 and CO is then defined as 2.75. It was found that the production rates of oxygenates obey well the same trend as the

coexistence of the CH_4 and CO value change. Even though the apparent production rates alone are not sufficient to further discuss the causality, a strong correlation between the two can be confirmed. As a similar phenomenon and trend can be observed in both the electrochemical tandem CO_2RR and the isotope co-reduction experiments, our study suggests possible asymmetric coupling pathways for multicarbon products, which leads to a catalytic selectivity shift towards oxygenates.

Discussion

From this study, we envision that various tandem systems can be devised for a more efficient and selective electrocatalytic CO_2-to-multicarbon oxygenate conversion, benefiting from asymmetric coupling inspired by the WL pathway. Thus far, there have been remarkable advances in the development of efficient CO-producing (that is, carbonyl branch) catalysts[49]. However, conventional Cu-based catalysts typically require large overpotentials for $*CH_x$ generation. Therefore, it is important to develop improved catalysts (that is, methyl branch catalysts) with reaction sites that not only can achieve an efficient production of $*CH_x$ intermediates with a high surface coverage at low overpotentials, but also can facilitate asymmetric coupling for a selective multicarbon oxygenate product generation. In addition, systematic optimizations are needed for the spatial distribution of two distinct catalysts in a tandem system and for the production rates of the two intermediates to attain improved catalytic results. Furthermore, microkinetic modelling studies are desired to scrutinize the impact of a microenvironment created by such tandem systems on the catalytic selectivity.

In summary, inspired by the WL metabolic pathway, we explored asymmetric C–C coupling in CO_2RR by both isotope-labelled co-reduction experiments and Cu–Ag electrochemical tandem catalysis in more practical CO_2 electroreduction conditions. We initially validated the characteristic catalysis process of $*CH_3$–*CO asymmetric coupling on a Cu surface. As it is challenging to directly probe the C–C coupling intermediate species, we developed an isotope-labelled co-reduction process to explore the $*CH_3$–*CO coupling on Cu. Within a wide potential window, asymmetric $*CH_3$–*CO coupling can happen on Cu and yield up to four detectable isotope-labelled oxygenate products, which include acetaldehyde, ethanol, acetic acid and acetone. Hydrogenation is necessary for the production of acetaldehyde and ethanol from the asymmetric coupling intermediate, whereas acetic acid and acetone are generated through an additional coupling process. After confirming the Cu-catalysed asymmetric C–C coupling in the model system, a Cu–Ag NP assembly was used as a tandem catalyst for CO_2 electroreduction to further explore the asymmetric coupling in more practical conditions. The production rate of the $*CH_x$ and *CO intermediates during CO_2RR can be successfully tuned by varying the NP number (and thus mass) ratio between Cu and Ag in the tandem system. The final generation rates of oxygenates were found to be strongly correlated with the coexistence of both intermediates. A maximized oxygenate generation rate can be achieved when those of the two intermediates are broadly aligned. These new insights of the C–C coupling pathway in CO_2 fixation not only confirmed the existence of asymmetric coupling as another pathway in addition to the well explored *CO–*CO symmetric coupling pathway, but also shed light on the new design paradigm of tandem catalytic systems in future CO_2 electrolysis.

Methods

Materials

Commercial Cu foil (thickness 0.25 mm, 99.98% trace metals basis), D_2O (99.9 atom% D), methyl iodide (contains Cu wire as the stabilizer, 99.5%), *o*-phosphoric acid (85%, Supelco), carbon rod (length 150 mm, diameter 6 mm, 99.995% trace metals basis), $KHCO_3$ (ACS reagent, 99.7%), K_2CO_3 (99.995% trace metals basis), KOH (99.99% trace metals basis), dimethyl sulfoxide (DMSO, ACS reagent, ≥99.9%), KI (ACS reagent, ≥99.0%) and airbags (Supel inert multilayer foil) were purchased from Sigma-Aldrich. Commercial Ag foil (thickness 0.28 mm, 99.9% trace metals basis) and Pt gauze (99.9% metal basis) were ordered from Alfa Aesar. Glassy carbon electrodes (CHI104) and Ag/AgCl (3 M KCl) reference electrodes were purchased from CH Instruments and World Precision Instruments, respectively. Glassy carbon plates (25 mm × 25 mm) were purchased from SPI supplies, and a glassy carbon planchet (diameter 25 mm) was purchased from Ted Pella. CO (4.0 research), CO_2 (4.5LS) and Ar gas were purchased from Praxair. Deionized (DI) water (with 18.2 MΩ cm, <5 ppb total organic carbon) was obtained from a Millipore water system. Isotope-labelled $^{13}CH_3I$ (99%) was purchased from Cambridge Isotope Laboratories, Inc. Fumasep and Selemion AMV anion exchange membrane were ordered from Fuel Cell Store and AGC Engineering, respectively.

Electrode preparation

The electrochemical polish parameter in the previous report[50] was used here. Specifically, the as-received Cu foil was first cut to the desired size, then sonicated in an ethanol bath and a DI water bath sequentially to remove the organic contamination on the Cu surface. Then, the Cu foil was dipped into the 85% *o*-phosphoric acid and electrochemically polished with a carbon rod as the counter electrode. The electrochemical polish process lasted for 10 min under an applied potential of 2.1 V versus the carbon rod. After the electrochemical polish, Cu foil was rinsed with DI water to remove acid on the surface and then blow-dried with Ar flow. The prepared EC-Cu was then immediately used for the characterization of electrochemical tests.

For Cu and Ag NP synthesis, previously reported recipes were followed[44–46]. NPs were spin coated on the glassy carbon planchet, and this process was optimized to load NPs close to a monolayer. To form a tandem NP system, Cu and Ag NP solutions were mixed and spin coated on the support by using a spin coater (Laurell WS-400A-6NPP/LITE). For instance, to make Cu50Ag50 where 50% of the total number of NPs was Cu NPs, the concentration of each Cu and Ag NP solution was taken into account when a mixed solution was prepared. The active area of the electrode exposed to the electrolyte was 1.13 cm^2.

Characterization

The images of Cu surface morphology were acquired by using an FEI Quanta 3D FEG/FIB SEM with the operation conditions of 5 kV and 3.4 nA. XPS (Thermo Scientific K-Alpha) characterization was conducted using an Al Kα source. To measure the post-electrolysis sample, EC-Cu foil was sampled after CH_3I and CO co-reduction under −0.8 V versus RHE for 6 h. The foil was then rinsed with DI water to remove as much electrolyte residue as possible and blow-dried with Ar flow. Post-electrolysis SEM images of the Cu–Ag NPs were directly collected on the glassy carbon substrate after the CO_2RR finished. For TEM-based characterizations, particles were redispersed in ethanol by ultrasonication, then deposited on the TEM grids. Atomic-scale high-angle annular dark-field detector STEM images and elemental EELS maps were acquired on a fifth-order aberration-corrected STEM (Cornell Nion UltraSTEM) operated at 100 keV with a beam convergence semi-angle of 30 mrad. Sub-ångström spatial resolution was achievable under such operating conditions. EELS spectral images were acquired with a 0.25 eV per channel energy dispersion (energy resolution, 1.0 eV) in a Gatan spectrometer with a size of 100 pixels and an acquisition time of 10 ms per pixel. EELS spectrum images were processed using principal component analysis (three components) and the linear combination of power law to subtract the background in ImageJ software. In addition, EDX mapping was acquired in a STEM mode using the Titan Themis microscope at the National Center for Electron Microscopy at LBNL. STEM–EDX maps were acquired for 30–40 min with drift correction using the Velox software and an estimated spatial resolution of 1–2 nm at 300 keV and about a 0.6 nA beam current using a quadruple Bruker EDX detector with a large solid angle of 0.7 steradian. High-resolution bright-field TEM images were also acquired on a Themis at 300 keV.

Electrochemical tests

Electrochemical tests were conducted in conventional H-cells. For all the CH_3I- and CO-related experiments, the cathode and anode of the H-cell were separated by an anion exchange membrane. The volume of electrolyte in both chambers was 50 ml. Before electrolysis, the electrolyte was first bubbled with carrier gases for at least 20 min to remove dissolved oxygen. $KHCO_3$ (0.1 M) was used as the default electrolyte unless specific conditions are stated. The gas flow rate during electrolysis was controlled at 10 ml min^{-1} by a mass flow controller at room temperature. Ag/AgCl (3 M KCl) was used as the reference electrode. For NP-based CO_2RR experiments, the volume of the electrolyte in both chambers was 17 ml and the gas flow rate was 20 ml min^{-1}. Besides that, other operating conditions and procedures were identical.

In double-layer capacitance measurements, the gas flow and stir bar were stopped after the system was fully deoxygenated. Meanwhile, the gas outlet was also sealed. The potential range of cyclic voltammetry scans was set from −0.1 to 0.25 V versus RHE. Through linear regression, the slope of the charging and discharging currents with respect to the scan rates was obtained, which corresponds to the surface's double-layer capacitance.

The polarization response curves were also collected with a cyclic voltammetry technique. After the cyclic voltammetry curve was stable (usually after five loops), the cathodic scan sections between 0.1 and −0.9 V versus RHE were then collected and plotted for comparison. CH_3I (10 µl) was added to the electrolyte to investigate the characteristic reduction peak and operation window of CH_3IRR.

Catalytic performances were tested with 85% iR compensated chronoamperometry. The remaining 15% iR drop was manually compensated during the data analysis. The deviation of actual potential from expected potential is normally smaller than 25 mV, which is not supposed to influence any of the comparison or conclusions in this study relative to the 200 or 150 mV intervals applied in the electrochemical tests. For both the ^{12}CO and $^{13}CH_3I$ co-reduction and $^{12}CO_2$ and $^{13}CH_3I$ co-reduction experiments, while the gas flow was kept constant during the 6 h electrolysis, two doses of 50 µl of CH_3I were added to the cathodic chamber at 0 and 3 h, respectively. The hazards associated with handling CH_3I (that is, volatile and highly toxic) require that all the CH_3I-relevant operations need to be performed in a fume hood accordingly. During each 3 h electrolysis period, the current gradually decreased due to the consumption of the CH_3I reduction as well as CH_3I evaporation with gas flow. All the gases that eluted from the outlet were cumulated in a gas bag during the electrolysis to obtain an averaged result. Liquid products were sampled after 6 h of electrolysis. For the CORR without CH_3I, gas was directly sampled from headspace with a syringe, so a gas bag is not necessary. In the KI-involved control experiment, 267 mg of fresh KI was dissolved in the catholyte to match up with the fed-in iodine in the co-reduction experiments. Other than the addition of KI, the set-up and operations of the control experiment were all the same as those for routine CORRs.

Product analysis

After electrolysis, gas products, which included CO, CH_4, C_2H_4, C_2H_6 and H_2 were detected and quantified using GC (Agilent 7890B GC system). An additional 10 min baking at 200 °C was added into the GC program to remove the CH_3I vapour trapped in the column. For NP-based CO_2 electrolysis gas products were measured by GC (SRI MG3) equipped with a thermal conductivity detector and a flame ionization detector. Liquid products were analysed by ^1H NMR spectroscopy (Bruker AV600 with a 5 mm Z-gradient triple resonance ^1H/BB Prodigy cryoprobe) with water suppression by excitation sculpting. 900 µl aliquot of the liquid and 100 µl of DMSO–D_2O solution were mixed for locking purposes, in which DMSO was used as the internal standard for quantification.

Data availability

All data is available from the authors upon reasonable request.

References

1. Jordaan, S. M. & Wang, C. Electrocatalytic conversion of carbon dioxide for the Paris goals. *Nat. Catal.* **4**, 915–920 (2021).
2. Ross, M. B. et al. Designing materials for electrochemical carbon dioxide recycling. *Nat. Catal.* **2**, 648–658 (2019).
3. Habisreutinger, S. N., Schmidt-Mende, L. & Stolarczyk, J. K. Photocatalytic reduction of CO_2 on TiO_2 and other semiconductors. *Angew. Chem. Int. Ed.* **52**, 7372–7408 (2013).
4. Jasniewski, A. J., Lee, C. C., Ribbe, M. W. & Hu, Y. Reactivity, mechanism, and assembly of the alternative nitrogenases. *Chem. Rev.* **120**, 5107–5157 (2020).
5. Marques Mota, F. & Kim, D. H. From CO_2 methanation to ambitious long-chain hydrocarbons: alternative fuels paving the path to sustainability. *Chem. Soc. Rev.* **48**, 205–259 (2019).
6. Can, M., Armstrong, F. A. & Ragsdale, S. W. Structure, function, and mechanism of the nickel metalloenzymes, CO dehydrogenase, and acetyl-CoA synthase. *Chem. Rev.* **114**, 4149–4174 (2014).
7. Ragsdale, S. W. & Pierce, E. Acetogenesis and the Wood–Ljungdahl pathway of CO_2 fixation. *Biochim. Biophys. Acta* **1784**, 1873–1898 (2008).
8. Nitopi, S. et al. Progress and perspectives of electrochemical CO_2 reduction on copper in aqueous electrolyte. *Chem. Rev.* **119**, 7610–7672 (2019).
9. Hori, Y., Murata, A. & Takahashi, R. Formation of hydrocarbons in the electrochemical reduction of carbon dioxide at a copper electrode in aqueous solution. *J. Chem. Soc. Faraday Trans. 1* **85**, 2309–2326 (1989).
10. Montoya, J. H., Shi, C., Chan, K. & Norskov, J. K. Theoretical insights into a CO dimerization mechanism in CO_2 electroreduction. *J. Phys. Chem. Lett.* **6**, 2032–2037 (2015).
11. Wang, L. et al. Electrochemical carbon monoxide reduction on polycrystalline copper: effects of potential, pressure, and pH on selectivity toward multicarbon and oxygenated products. *ACS Catal.* **8**, 7445–7454 (2018).
12. Hanselman, S., Koper, M. T. M. & Calle-Vallejo, F. Computational comparison of late transition metal (100) surfaces for the electrocatalytic reduction of CO to C_2 species. *ACS Energy Lett.* **3**, 1062–1067 (2018).
13. Perez-Gallent, E., Figueiredo, M. C., Calle-Vallejo, F. & Koper, M. T. Spectroscopic observation of a hydrogenated CO dimer intermediate during CO reduction on Cu(100) electrodes. *Angew. Chem. Int. Ed.* **56**, 3621–3624 (2017).
14. Kim, Y. et al. Time-resolved observation of C–C coupling intermediates on Cu electrodes for selective electrochemical CO_2 reduction. *Energy Environ. Sci.* **13**, 4301–4311 (2020).
15. Xiao, H., Cheng, T., Goddard, W. A. & Sundararaman, R. Mechanistic explanation of the pH dependence and onset potentials for hydrocarbon products from electrochemical reduction of CO on Cu(111). *J. Am. Chem. Soc.* **138**, 483–486 (2016).
16. Xiao, H., Cheng, T. & Goddard, W. A. Atomistic mechanisms underlying selectivities in C_1 and C_2 products from electrochemical reduction of CO on Cu(111). *J. Am. Chem. Soc.* **139**, 130–136 (2017).
17. Zhao, Q., Martirez, J. M. P. & Carter, E. A. Revisiting understanding of electrochemical CO_2 reduction on Cu(111): competing proton-coupled electron transfer reaction mechanisms revealed by embedded correlated wavefunction theory. *J. Am. Chem. Soc.* **143**, 6152–6164 (2021).
18. Ma, W. et al. Electrocatalytic reduction of CO_2 to ethylene and ethanol through hydrogen-assisted C–C coupling over fluorine-modified copper. *Nat. Catal.* **3**, 478–487 (2020).

19. Choi, C. et al. Highly active and stable stepped Cu surface for enhanced electrochemical CO_2 reduction to C_2H_4. *Nat. Catal.* **3**, 804–812 (2020).
20. Garza, A. J., Bell, A. T. & Head-Gordon, M. Mechanism of CO_2 reduction at copper surfaces: pathways to C_2 products. *ACS Catal.* **8**, 1490–1499 (2018).
21. Schouten, K. J., Qin, Z., Perez Gallent, E. & Koper, M. T. Two pathways for the formation of ethylene in CO reduction on single-crystal copper electrodes. *J. Am. Chem. Soc.* **134**, 9864–9867 (2012).
22. Cheng, T., Xiao, H. & Goddard, W. A. Full atomistic reaction mechanism with kinetics for CO reduction on Cu(100) from ab initio molecular dynamics free-energy calculations at 298 K. *Proc. Natl Acad. Sci. USA* **114**, 1795–1800 (2017).
23. Dinh, C.-T. et al. CO_2 electroreduction to ethylene via hydroxide-mediated copper catalysis at an abrupt interface. *Science* **360**, 783–787 (2018).
24. Luc, W. et al. Two-dimensional copper nanosheets for electrochemical reduction of carbon monoxide to acetate. *Nat. Catal.* **2**, 423–430 (2019).
25. Kim, C. et al. Tailored catalyst microenvironments for CO_2 electroreduction to multicarbon products on copper using bilayer ionomer coatings. *Nat. Energy* **6**, 1026–1034 (2021).
26. Vasileff, A. et al. Electrochemical reduction of CO_2 to ethane through stabilization of an ethoxy intermediate. *Angew. Chem. Int. Ed.* **132**, 19817–19821 (2020).
27. Ren, D., Ang, B. S.-H. & Yeo, B. S. Tuning the selectivity of carbon dioxide electroreduction toward ethanol on oxide-derived Cu_xZn catalysts. *ACS Catal.* **6**, 8239–8247 (2016).
28. Iyengar, P., Kolb, M. J., Pankhurst, J. R., Calle-Vallejo, F. & Buonsanti, R. Elucidating the facet-dependent selectivity for CO_2 electroreduction to ethanol of Cu–Ag tandem catalysts. *ACS Catal.* **11**, 4456–4463 (2021).
29. Ting, L. R. L. et al. Enhancing CO_2 electroreduction to ethanol on copper–silver composites by opening an alternative catalytic pathway. *ACS Catal.* **10**, 4059–4069 (2020).
30. Raaijman, S. J., Schellekens, M. P., Corbett, P. J. & Koper, M. T. M. High-pressure CO electroreduction at silver produces ethanol and propanol. *Angew. Chem. Int. Ed.* **60**, 21732–21736 (2021).
31. Kas, R. et al. In-situ infrared spectroscopy applied to the study of the electrocatalytic reduction of CO_2: theory, practice and challenges. *ChemPhysChem* **20**, 2904–2925 (2019).
32. Sebastián-Pascual, P. & Escudero-Escribano, M. Surface characterization of copper electrocatalysts by lead underpotential deposition. *J. Electroanal. Chem.* **896**, 115446 (2021).
33. Chen, Y. Recent advances in methylation: a guide for selecting methylation reagents. *Chem. Eur. J.* **25**, 3405–3439 (2019).
34. Zhang, W. et al. Electrochemically driven cross-electrophile coupling of alkyl halides. *Nature* **604**, 292–297 (2022).
35. Fedurco, M., Sartoretti, C. J. & Augustynski, J. Reductive cleavage of the carbon–halogen bond in simple methyl and methylene halides. Reactions of the methyl radical and carbene at the polarized electrode/aqueous solution interface. *Langmuir* **17**, 2380–2387 (2001).
36. Lin, J. L. & Bent, B. E. Two mechanisms for formation of methyl radicals during the thermal decomposition of methyl iodide on a copper surface. *J. Phys. Chem.* **97**, 9713–9718 (1993).
37. Lei, C., Liang, F., Li, J., Chen, W. & Huang, B. Electrochemical reductive dechlorination of chlorinated volatile organic compounds (Cl-VOCs): effects of molecular structure on the dehalogenation reactivity and mechanisms. *Chem. Eng. J.* **358**, 1054–1064 (2019).
38. Gunathunge, C. M., Ovalle, V. J., Li, Y., Janik, M. J. & Waegele, M. M. Existence of an electrochemically inert CO population on Cu electrodes in alkaline pH. *ACS Catal.* **8**, 7507–7516 (2018).
39. Li, J., Li, X., Gunathunge, C. M. & Waegele, M. M. Hydrogen bonding steers the product selectivity of electrocatalytic CO reduction. *Proc. Natl Acad. Sci. USA* **116**, 9220–9229 (2019).
40. Chang, X., Malkani, A., Yang, X. & Xu, B. Mechanistic insights into electroreductive C–C coupling between CO and acetaldehyde into multicarbon products. *J. Am. Chem. Soc.* **142**, 2975–2983 (2020).
41. Van Santen, R., Markvoort, A., Filot, I., Ghouri, M. & Hensen, E. Mechanism and microkinetics of the Fischer–Tropsch reaction. *Phys. Chem. Chem. Phys.* **15**, 17038–17063 (2013).
42. Zhao, Y. et al. Direct C–C coupling of CO_2 and the methyl group from CH_4 activation through facile insertion of CO_2 into $Zn–CH_3$ σ-bond. *J. Am. Chem. Soc.* **138**, 10191–10198 (2016).
43. Zhao, Y., Wang, H., Han, J., Zhu, X. & Ge, Q. Active site ensembles enabled C–C coupling of CO_2 and CH_4 for acetone production. *J. Phys. Chem. C* **122**, 9570–9577 (2018).
44. Kim, D. et al. Selective CO_2 electrocatalysis at the pseudocapacitive nanoparticle/ordered-ligand interlayer. *Nat. Energy* **5**, 1032–1042 (2020).
45. Hung, L. I., Tsung, C. K., Huang, W. & Yang, P. Room-temperature formation of hollow Cu_2O nanoparticles. *Adv. Mater.* **22**, 1910–1914 (2010).
46. Kim, D., Kley, C. S., Li, Y. & Yang, P. Copper nanoparticle ensembles for selective electroreduction of CO_2 to C_2–C_3 products. *Proc. Natl Acad. Sci. USA* **114**, 10560–10565 (2017).
47. Manthiram, K., Beberwyck, B. J. & Alivisatos, A. P. Enhanced electrochemical methanation of carbon dioxide with a dispersible nanoscale copper catalyst. *J. Am. Chem. Soc.* **136**, 13319–13325 (2014).
48. Huang, J., Mensi, M., Oveisi, E., Mantella, V. & Buonsanti, R. Structural sensitivities in bimetallic catalysts for electrochemical CO_2 reduction revealed by Ag–Cu nanodimers. *J. Am. Chem. Soc.* **141**, 2490–2499 (2019).
49. Gu, J., Hsu, C.-S., Bai, L., Chen, H. M. & Hu, X. Atomically dispersed Fe^{3+} sites catalyze efficient CO_2 electroreduction to CO. *Science* **364**, 1091–1094 (2019).
50. Wang, L. et al. Selective reduction of CO to acetaldehyde with CuAg electrocatalysts. *Proc. Natl Acad. Sci. USA* **117**, 12572–12575 (2020).

Acknowledgements

This work was supported by the Director, Office of Science, Office of Basic Energy Sciences, Chemical Sciences, Geosciences and Biosciences Division of the US Department of Energy under contract DE-AC02-05CH11231, FWP CH030201 (Catalysis Research Program). STEM–EDX and XPS were conducted using facilities at the Molecular Foundry. Work at the Molecular Foundry was supported by the Office of Science, Office of Basic Energy Sciences of the US Department of Energy under contract no. DE-AC02-05CH11231. The STEM–EELS work made use of the TEM facilities (Nion UltraSTEM) at the Cornell Center for Materials Research (CCMR), which are supported through the National Science Foundation Materials Research Science and Engineering Center (NSF MRSEC) program (DMR-1719875). We thank the TEM technical support of R. Dhall and K. Bustillo at NCEM and of M. Thomas at Cornell. We thank H. Celik and UC Berkeley's NMR facility in the College of Chemistry (CoC-NMR) for spectroscopic assistance. Instruments in the CoC-NMR are supported in part by NIH S10OD024998. C.C. and J.J. gratefully acknowledge support from Suzhou Industrial Park Scholarships. S.Y. acknowledges support from a Samsung Scholarship. Y.Y. acknowledges support from a Miller Research Fellowship. P.-C.C. acknowledges support from a Kavli ENSI Heising-Simons Fellowship.

Author contributions

C.C., S.Y. and P.Y. conceived the research and designed the experiments. C.C. conducted the isotope labelling experiments and S.Y. conducted the NP synthesis and CO_2 electrolysis with assistance from S.L., I.R., S.C. and Y.S. Electron microscopy characterization and structural analysis were conducted by Y.Y., J.J. and P.-C.C. All the authors contributed to the discussion of the experimental results and the preparation of the manuscript.

Competing interests

The authors declare no competing interests.

Additional information

Supplementary information The online version contains supplementary material available at https://doi.org/10.1038/s41929-022-00844-w.

Correspondence and requests for materials should be addressed to Peidong Yang.

Peer review information *Nature Catalysis* thanks Bo Yang, Xinli Zhu and the other, anonymous, reviewer(s) for their contribution to the peer review of this work.